Planetary and Space Science 113-114 (2015) 298–308

Contents lists available at ScienceDirect

Planetary and Space Science

journal homepage: www.elsevier.com/locate/pss

The radiative forcing variability caused by the changes of the upper cloud vertical structure in the Venus mesosphere

Y.J. Lee [a,b,*], D.V. Titov [c], N.I. Ignatiev [d], S. Tellmann [e], M. Pätzold [e], G. Piccioni [f]

[a] Institute of Space and Astronautical Science (ISAS), Japan Aerospace Exploration Agency (JAXA), Sagamihara, Japan
[b] Max Planck Institute for Solar System Research, Göttingen, Germany
[c] ESA/ESTEC, Noordwijk, The Netherlands
[d] Space Research Institute (IKI), Moscow, Russia
[e] Rheinish Institute for Environmental Research, Universität zu Köln, Cologne, Germany
[f] INAF-IAPS, Rome, Italy

ARTICLE INFO

Article history:
Received 30 March 2014
Received in revised form
6 October 2014
Accepted 4 December 2014
Available online 18 December 2014

Keywords:
Venus
Mesosphere
Clouds
Radiative energy balance

ABSTRACT

The upper cloud layer of Venus is a key factor affecting radiative energy balance of the mesosphere. Observations of the temperature and the cloud top structure by Venus Express revealed their strong variability with latitude. We used the 1-D radiative transfer model to study the dependence of the radiative forcing on the cloud top structure. The cloud top altitude effectively controls outgoing thermal fluxes. Sharp cloud top boundary can produce a pronounced peak of both solar heating and thermal cooling that suggests a radiative origin of temperature inversions in the cold collar. Strong diurnal variation of net forcing at low latitudes can be responsible for the origin of convective cells observed in UV images. Latitudinal contrasts in the radiative forcing in the mesosphere can drive meridional Hadley-type circulation with meridional winds of few m/s and vertical motions with speed of few cm/s.

1. Introduction

Venus receives twice the solar flux (2622 W/m^2) of the Earth (Moroz et al., 1985). However, the thick cloud deck that completely shrouds the planet reflects most of the solar radiation back to space, allowing only 2.5–3.4% of total solar flux to reach the surface (Tomasko et al., 1980b; Moroz et al., 1983). Almost half of the incoming flux is absorbed by the unknown UV absorber in the upper cloud layer above ~60 km (Crisp, 1986). Also the clouds produce high opacity in the long wavelength range. Hot Venus surface (735 K) has strong emission in thermal infrared range absorbed by the clouds and atmospheric gases. The clouds are the second strongest greenhouse agent in the Venus atmosphere after CO_2 (Bullock, 1997; Titov et al., 2007). As a result, the clouds are very important factor in the radiative energy balance of the Venus atmosphere.

The vertical structure of the clouds was investigated in situ by Venera 8–14 landers and four Pioneer Venus descent probes (Ragent et al., 1985). These data sets suggested that the main cloud deck (~48–70 km) is divided into lower, middle, and upper cloud layers (Knollenberg and Hunten, 1980; Ragent et al., 1985). The tropopause is located at around 60 km altitude at the base of the upper cloud layer (Tellmann et al., 2009). There is a clear trend for the cloud top altitude to decrease from equator toward the poles (Zasova et al., 2007; Ignatiev et al., 2009; Lee et al., 2012; Haus et al., 2014). The cloud top is defined as the level of the unity optical thickness at 4–5 μm, is located at 67 km in low latitude region and descends to 63 km at the poles (Lee et al., 2012). The aerosol scale height also decreases with latitude from 4 km at low latitudes to 1.7 km in the polar regions (Zasova et al., 2007; Lee et al., 2012).

The previous radiative energy balance calculations could successfully reproduce the observed flux profiles (Tomasko et al., 1980a,b; Crisp, 1986). These models calculated globally averaged solar heating and thermal cooling rates, showing peaks of radiative forcing near the cloud tops of 6–10 K/Earth-day for the solar heating, and of 6–7 K/Earth-day for the thermal cooling (Tomasko et al., 1985; Crisp, 1986, 1989; Crisp and Titov, 1997). They also demonstrated dependence of the radiative forcing on the cloud top structure and vertical distribution of the UV absorbers.

Since the upper cloud plays an important role in the solar heating and thermal cooling, variations of the cloud top structure strongly affect radiative forcing of the Venus mesosphere. This may be related to several unsolved questions in dynamic and physical phenomena in the Venus mesosphere. Firstly, the strong retrograde zonal wind ('super-rotation') has the maximum speed near the cloud top (Gierasch et al., 1997) exceeding by more than a factor of 50 that of the solid body rotation. Thus, air parcels can travel around

* Corresponding author at: Institute of Space and Astronautical Science (ISAS), Japan Aerospace Exploration Agency (JAXA), Sagamihara, Japan.
E-mail address: leeyj@ac.jaxa.jp (Y.J. Lee).

http://dx.doi.org/10.1016/j.pss.2014.12.006
0032-0633/

the globe in about four Earth-days (Taylor, 2006). Thermal tides forced by the solar heating at the cloud top are one of the possible mechanisms maintaining the super-rotation (Gierasch et al., 1997; Takagi and Matsuda, 2007; Lebonnois et al., 2010), but the exact mechanism is not fully understood yet. Secondly, polar vortices show significant morphological changes with time. The energy sources of the polar vortices are thought to be solar energy deposition at the cloud top on the day side and the absorption of thermal energy at the cloud base (Limaye, 2007). Thirdly, some features of the temperature structure at the cloud top have not yet been fully explained. One of them is strong temperature inversions at the cloud top at high latitudes with temperatures about 30 K colder than the same altitude at the equator. Another feature is the warm polar mesosphere at 75–90 km that is probably related to adiabatic warming due to downwelling branch of the Hadley circulation (Taylor, 2006; Migliorini et al., 2012).

We calculated vertical distribution of thermal and solar flux using recent results on the cloud top and temperature structure from Venus Express (Tellmann et al., 2009; Lee et al., 2012). One-dimensional radiative transfer model was used for a set of latitudinal and local time bins. We also studied sensitivity of the radiative modelling to the cloud top structure to understand its role in the radiative forcing (Tomasko et al., 1985; Crisp, 1986, 1989). In Section 2 we describe the input data and computing methods. In Section 3 we derive variations of the cooling and heating rates caused by the cloud top structure variations. Meridional trends in the net radiative energy balance are revealed, providing insights in the mechanisms of mesospheric circulation (Taylor et al., 1983; Crisp, 1989; Crisp and Titov, 1997; Titov et al., 2007). The last section concludes on results and plans for future studies.

2. Data and methods

Radiative forcing strongly depends on the temperature and cloud structures. Here we describe the data used in this study to update the atmospheric model. Radiative flux calculations used to derive thermal cooling and solar heating rates are described in the later subsections.

2.1. Atmospheric model

The entire lower atmosphere (0–100 km) is considered in this study. The atmospheric model is based on the temperature, pressure, and cloud top structure derived from results of the previous space missions and updated by the Venus Express observations. The gaseous absorption of CO_2 requires careful consideration due to very high pressure in the deep atmosphere. Clouds are represented by a four mode aerosol size distribution. The upper cloud vertical structure derived by Lee et al. (2012) is incorporated in our cloud model.

2.1.1. Temperature and pressure profiles

Temperature sounding by the radio-occultation experiment (VeRa) on board Venus Express was used to derive temperature and pressure fields in the upper troposphere and mesosphere (50–95 km) (Häusler et al., 2006; Pätzold et al., 2007; Tellmann et al., 2009). The VeRa experiment provided atmospheric temperature structure with high vertical resolution and good spatial coverage. We distributed 133 VeRa profiles obtained from 2006 to 2010, in 18 latitudinal bins from equator to the south pole as shown in Table 1. We neglected the local time variability of the temperature structure compared to the meridional variation and averaged the profiles in each bin (see Lee et al., 2012, Fig. 2). This allowed us to focus on the effects of the latitudinal cloud top structure variability. Below 50 km we used the Venus International Reference Atmosphere (VIRA) model based on several in situ measurements onboard the Venera landers and Pioneer Venus probes (Seiff et al., 1985). Five latitudinal bins of the VIRA data were linearly interpolated into the 18 latitudinal bins selected in this study. A discontinuity, between the two data sets at 50 km, was smoothened by a running average (Chapman, 2007) in the 48–52 km altitude range. Also VIRA profiles were used above 95 km.

Table 1
Parameters of the upper cloud as a function of latitude used in the cloud model (Lee et al., 2012).

Latitude range (°S)	Z (km)	H (km)
0–5	68.1	4.0
5–10	67.6	5.0
10–15	68.2	3.9
15–20	67.8	4.3
20–25	68.3	3.5
25–30	68.4	4.0
30–35	67.4	3.7
35–40	67.6	3.7
40–46	67.0	4.1
46–50	64.0	3.4
50–56	67.3	3.3
56–60	66.0	3.1
60–65	64.5	2.6
65–70	65.1	1.7
70–75	63.5	1.5
75–80	64.6	2.1
80–85	63.1	1.6
85–90	62.3	1.8

Fig. 1 shows examples of temperature and pressure profiles for three latitudinal bins. The atmospheric structure does not depend on latitude below 33 km. Above this altitude the temperature profiles show clear latitudinal dependence. At low latitudes atmospheric temperature decreases monotonically with altitude (Fig. 1a). Poleward from ~45°S a strong temperature inversion layer exists near the cloud top (Pätzold et al., 2007) forming the so-called “cold collar” region. In the polar region the mesosphere is warmer than at low latitudes resulting in inverse meridional temperature gradient.

2.1.2. Atmospheric gaseous absorption

The atmospheric model considers opacities of CO_2, H_2O, and SO_2. CO_2 is well-mixed in the atmosphere with abundance of 96.5%. The vertical distributions of H_2O and SO_2 were taken from Titov et al. (2007). We used line parameters from the HITRAN2008 database (Rothman et al., 2009). High atmospheric pressure and large amount of CO_2 result in that the CO_2 bands play a very important role in the radiative energy balance. In addition, strong pressure broadening of CO_2 requires correction of Lorentz line shape factors. We used five empirical correction methods (Winters et al., 1964; Burch et al., 1969; Moskalenko and Parzhin, 1981; Tanaka and Yamanouchi, 1977; Pollack et al., 1993; Meadows and Crisp, 1996; Tonkov et al., 1996; Ignatiev et al., 1999). Each line shape factor was developed and used for particular CO_2 bands that was taken into account in this study. At wavenumbers below 2000 cm^{-1}, the line shape factor was taken from Ignatiev et al. (1999) (based on Moskalenko and Parzhin, 1981), which had been used for 250–1650 cm^{-1} range. Between 2000 cm^{-1} and 2600 cm^{-1}, we used the line shape factor from Winters et al. (1964). In the range from 2600 cm^{-1} to 3800 cm^{-1}, the formula was taken from Pollack et al. (1993), that followed the study of the collision-broadened CO_2 line shapes by Burch et al. (1969). In the range of 3800–4700 cm^{-1}, we used the formula from Tonkov et al. (1996), derived for the 2.3 μm spectral region at 296 K. At wavenumbers larger than 4700 cm^{-1}, we adopted the formula from Meadows and Crisp (1996) which fits the 2.3 μm and 1.74 μm

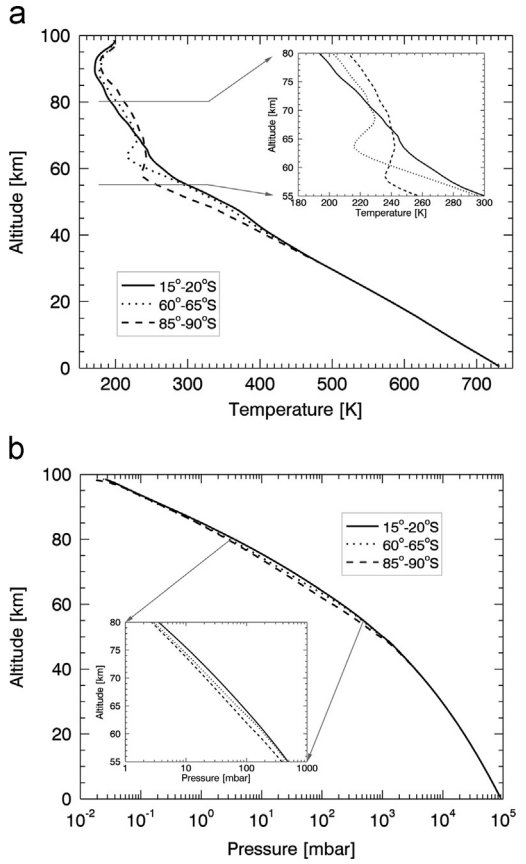

Fig. 1. (a) Model temperature profiles based on VeRa measurements above 50 km and VIRA models below. Three lines represent different latitudinal regions: low latitude (15°–20°S), the cold collar (60°–65°S), and the pole (85°–90°S). (b) Model pressure profiles for the same latitudinal regions. Inserts show details of temperature and pressure profiles in the 55–80 km altitude range.

spectral regions. The CO_2 absorption was calculated with the Voigt line profile using the cutoff value of 200 cm^{-1} and a self-broadening coefficient. For H_2O lines we used scaling factor of 1.7 to adjust the line half-width to the CO_2 dominated Venus atmosphere (Fedorova et al., 2008). For SO_2 we assumed the air-broadening half-width without any scaling factor due to lack of data. For gaseous absorptions of H_2O and SO_2 we used the cutoff value of 100 cm^{-1}. Rayleigh scattering in the Venus atmosphere was taken into account (Pollack, 1967; Hansen and Travis, 1974) as well as SO_2 absorption at UV wavelengths (Wu et al., 2000).

2.1.3. Cloud model

The main cloud deck consists of the upper (> 60 km), middle (50–60 km), and lower (48–50 km) cloud layers. We assumed sulfuric acid (75%) composition and four-mode aerosol size distribution for the cloud layers: mode 1 - the small size particles with $r < 0.2$ μm, mode 2 – the middle size particles with $r \sim 1.0$ μm, and mode 3 – the large size particles with $r \sim 3.8$ μm, as well as mode 2′ – $r \sim 1.4$ μm, based on the Pioneer Venus measurements (Knollenberg and Hunten, 1980; Pollack et al., 1980; Zasova et al., 2007). Optical properties of the aerosols were obtained by Mie code calculation (Palmer and Williams, 1975; Wiscombe, 1980). Since the number density of mode 2 is dominant in the upper cloud layer, we assumed that it contains only mode 2 particles, while the middle and lower clouds are combinations of mode 1, mode 2′ and mode 3 particles. For the upper cloud we used exponential vertical distribution following Lee et al. (2012),

$$E(z) = E_0 \exp[-(z - z_0)/H] \quad (1)$$

where $E(z)$ is the vertical profile of the volume extinction coefficient, H is the aerosol scale height, and E_0 is the extinction at z_0 (65 km) altitude. The cloud top altitude (Z) is defined as the height of the unit optical thickness ($z_{\tau=1}$) at 2000 cm^{-1} to keep consistency with analysis by Lee et al. (2012). Therefore, H and Z are the parameters that define the vertical structure of the upper cloud in this study. The structure of the middle and lower cloud layers is taken from Zasova et al. (2007) and assumed latitude independent. Fig. 2 shows the number density profiles.

Table 2 shows cloud parameters for the standard model in three latitude regions. We used this set of aerosol models to study dependence of radiative fluxes on the cloud structure. A range of H and Z was used in the sensitivity study. Table 1 shows the parameters of the cloud top structure for 18 latitude bins. The meridional trends of radiative forcing are calculated based on Table 1. The upper haze was not considered in this study.

2.1.4. Unknown UV absorber

The chemical composition and vertical distribution of the unknown UV absorber are not well understood. However, as it absorbs about half of the incoming solar flux (Crisp, 1986), it strongly affects solar heating. Therefore, this study employs several assumptions to take the unknown UV absorber into account. Firstly, the absorber is present in the upper cloud only. The unknown UV absorber is modelled by the reduction of single scattering albedo of mode 2 particles following the model of Tomasko et al. (1985). Thus, the vertical distribution of the unknown UV absorber follows that of the upper cloud structure. Secondly, we limited the presence of the unknown UV absorber to the layer between 58 km and the cloud top (Z km). A similar assumption was used in the previous studies (Pollack et al., 1979; Esposito, 1980; Tomasko et al., 1985; Crisp, 1986), resulting in a distinct solar heating at the cloud top.

Fig. 3 shows good agreement between calculated and measured flux profiles in the 0.4–1.0 μm range. Discrepancies can be explained by that the tropospheric gaseous absorption requires more

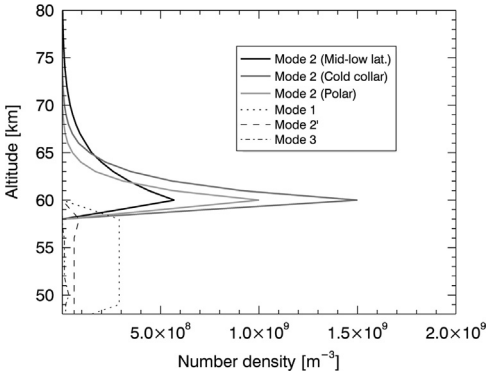

Fig. 2. Cloud model. Vertical profiles of aerosol number density for modes 1, 2, 2′, and 3. Number density for modes 1, 2′, and 3 below 60 km are taken from Zasova et al. (2007). The mode 2 profile is latitude dependent and is shown by three solid lines indicate for the low-to-middle latitudes, the cold collar, and the polar region (Table 2).

Table 2
Averaged parameters of the upper cloud in the model (Lee et al., 2012).

Latitude range	Low-to-mid (0°–56°S)	Cold collar (56°S–80°S)	Polar region (80°S–90°S)
Aerosol scale height (H, km)	3.8 ± 1.6	2.1 ± 2.0	1.7 ± 2.4
Cloud top altitude (Z, km)	67.2 ± 1.9	64.7 ± 3.2	62.8 ± 4.1

careful consideration, such as adding weak CO_2 lines not included in HITRAN2008, a greater cutoff values than what we used, and adjusting of H_2O abundance. The structure of the middle and lower cloud layers can be another source of the disagreement.

2.2. Radiative energy balance calculations

Calculations of the radiative energy balance include broad spectral range encompassing both thermal emission and solar radiation. This spectral range is divided into narrow spectral intervals for convenience. In these spectral intervals, monochromatic upward and downward flux profiles are calculated by a radiative transfer model and then integrated over wavelength followed by calculation of heating and cooling rates.

2.2.1. Spectral intervals

Solar spectrum has a maximum in the visible range and decreases quickly at $\lambda > 4\ \mu m$ ($< 2000\ cm^{-1}$). In the UV range, SO_2 and the unknown UV absorber are mainly responsible for absorption of the solar radiation. Fig. 4 compares Venus spherical albedo calculated in this study to the observations and previous modelling (Barker et al., 1975; Pollack et al., 1979; Tomasko et al., 1985). This demonstrates good agreement in the UV and visible spectral ranges including the SO_2 absorption feature. In the near infrared range, the absorptions by CO_2, H_2SO_4 aerosols, H_2O, and SO_2 become significant.

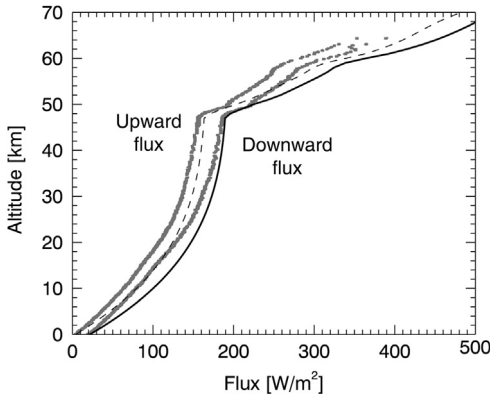

Fig. 3. Integrated flux profiles calculated in this study. Black solid and dashed lines are downward and upward fluxes, respectively. Grey line shows in situ total measurements onboard the Pioneer Venus descent probe (Tomasko et al., 1980b). The profiles correspond to 65.6° solar zenith angle.

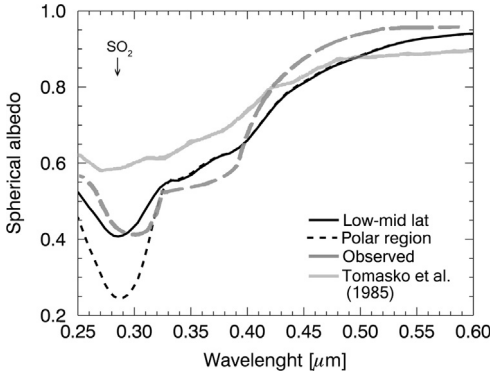

Fig. 4. Venus spherical albedo derived in this study and previous studies. Black solid and dashed lines show the albedo in the low-to-middle latitudes and the polar models. Grey dashed line shows the spectrum from Pollack et al. (1979) reconstructed from the ground-based (Barker et al., 1975) and satellite observations. The model by Tomasko et al. (1985) is also shown as light grey line.

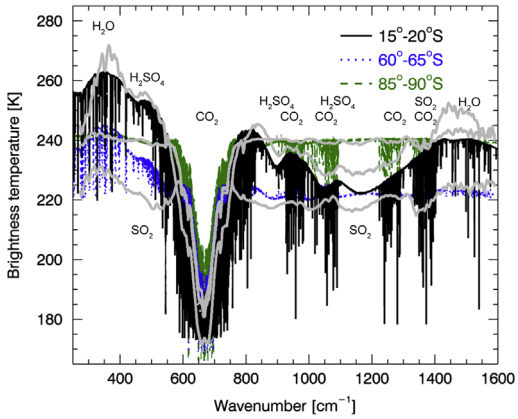

Fig. 5. Brightness temperature comparison of this study and previous observation analysis. Zenith direction thermal radiance at the top of our model are converted into brightness temperature. Gray lines are taken from Zasova et al. (2007) for the corresponding latitudes to the three regions.

Beyond 4–5 μm the radiative balance is dominated by thermal emission. The cloud opacity is high enough to trap the emission from the surface and deep atmosphere maintaining powerful greenhouse effect. Maximum of thermal emission is located at around 10 μm (1000 cm^{-1}) for the cloud top temperatures shifting to shorter wavelengths in the hot deep atmosphere. Infrared gaseous absorption by CO_2 is significant due to presence of strong absorption bands in this range and its high abundance. These features are demonstrated in Fig. 5, comparing synthetic thermal spectra of this study and observed spectra. The three latitudinal thermal structure shown in Fig. 1 and the cloud top structures at each latitudinal bin in Table 1 are used to calculate these spectra. This comparison shows that the conditions used in our study qualitatively well produce latitudinal characteristics.

This study considers two broad spectral ranges: 0.2–5.0 μm (2000–50000 cm^{-1}) for solar radiation and 3.9–200 μm (50–2590 cm^{-1}) for thermal radiation. Thermal emission leaking from the lower atmosphere in the near infrared transparency windows is not taken into account, since its contribution to the mesospheric radiative energy balance is negligible (Crisp and Titov, 1997). The broad ranges are divided into 6 and 7 spectral intervals for thermal and solar radiation respectively.

2.2.2. Flux calculations

The fast line-by-line calculation routine (Titov and Haus, 1997) was merged with the Spherical Harmonics Discrete Ordinate Method (SHDOM) (Evans, 1998) for this study. For each gas and spectral interval we calculated a matrix of gaseous absorption coefficients as a function of wavenumber, pressure, and temperature. The asymmetry factor for the Henyey–Greenstein phase function and single scattering albedo was calculated as weighted averages in the heterogeneous atmosphere with four-mode cloud model (Levoni et al., 1997). The solar spectral irradiance model[1] was scaled to the distance of 0.723 AU from the Sun. Surface albedo of 0.2 was assumed over the entire wavelength range. Downward and upward fluxes were calculated with 1 km step to get vertical profiles of the net flux. The monochromatic flux profiles were then spectrally integrated. And finally the radiative energy sources and sinks were derived as the divergence of the net flux (Goody and Yung, 1989). Fig. 6 demonstrates general agreement between the net flux divergence profiles obtained in our calculations and results in the earlier study (Lee and Richardson, 2011). Minor differences can be explained by differences in the atmospheric models.

[1] http://rredc.nrel.gov/solar/spectra/am0/modtran.html

The heating rate in [K/day] is expressed as follows:

$$\frac{dT}{dt} = \frac{1}{\rho c_p}(-\nabla \cdot \mathbf{F}_{\text{net}}) \quad (2)$$

where ρ is the density and c_p is the gas heat capacity at constant pressure. The divergence of the net flux ($\nabla \cdot \mathbf{F}_{\text{net}}$) can be replaced by $d\mathbf{F}_{\text{net}}/dz$, since we assume one-dimensional atmosphere. There is a notice that the thermal "cooling" in this study includes the negative sign.

For pure CO_2 atmosphere the specific heat at constant pressure (c_p, [J/(kg K)]) as a function of temperature is taken from Crisp (1986):

$$c_p(T) = 443.15 + 1.688T - 1.269 \times 10^{-3}T^2 + 3.47 \times 10^{-7}T^3. \quad (3)$$

Density in [kg/m^3] is derived from the ideal gas law,

$$\rho(z) = \frac{p(z)}{RT(z)} \quad (4)$$

where p is pressure in bar, T is the temperature in K, and $R = 191.4$ J/(kg K) is the universal gas constant in the Venus atmosphere with the mean molecular weight of 43.44 that corresponds to the composition of 96.5% CO_2, 3.5% N_2, 180 ppm SO_2, 60 ppm Ar and 30 ppm CO (Seiff et al., 1985).

3. Results

We performed modelling of the radiative energy balance in the Venus mesosphere. The following two sections show the thermal and solar range results separately. First, we explore the sensitivity of radiative fluxes on the cloud top structure. Second, we present meridional trends in thermal cooling and solar heating rates that define net meridional radiative forcing. The latitude dependent cloud top structure (Table 1) was used for the calculation of the second part.

3.1. Thermal emission

The sensitivity study is performed for three regions: the low-to-middle latitudes, the cold collar, and the polar regions. The temperature and pressure profiles for three latitudinal bins are shown in Fig. 1. The cloud top structure parameters were varied. The aerosol scale height changed between 1 and 6 km while the cloud top altitude ranged between 61 and 70 km (Lee et al., 2012) with one parameter varied at a time and the second one fixed to its mean value shown in Table 2.

Fig. 7a shows the dependence of the thermal fluxes on the cloud top altitude. As the cloud top altitude increases by 9 km, the outgoing thermal flux decreases by about 50 W/m^2, i.e. by one-third of the averaged total thermal emission from Venus to space (Moroz et al., 1985). This is due to monotonically decreasing temperature with altitude at low latitudes resulting in lower temperature of higher cloud tops. Fig. 7b shows the effect of the aerosol scale height on the flux profiles. Sensitivity of the outgoing thermal fluxes to the aerosol scale height is weaker for the low-to-middle latitude temperature structure. The outgoing emission ranges between 25 W/m^2 and 10 W/m^2 in the cold collar and the

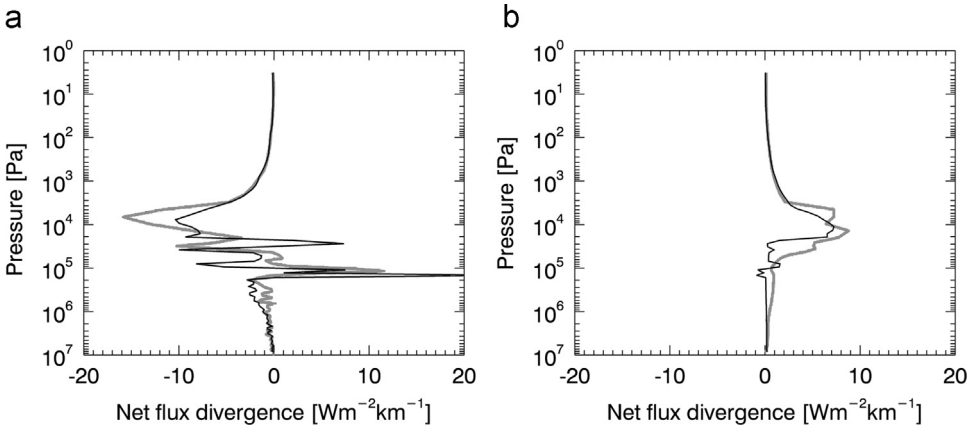

Fig. 6. Globally averaged net flux divergence comparisons of this study and previous calculation work. (a) Thermal flux and (b) solar flux are shown separately, and minus means cooling effect. The black lines are net flux divergence profile calculated in this work, and gray lines are taken from Lee and Richardson (2011).

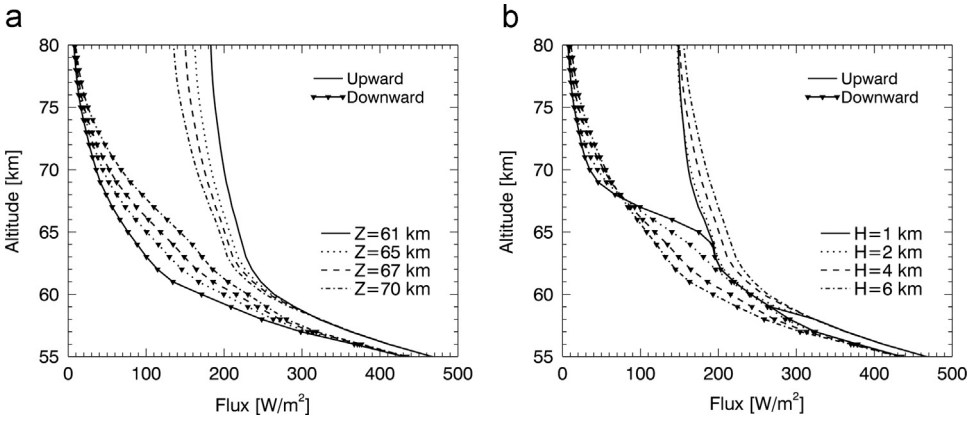

Fig. 7. Sensitivity of the upward and downward thermal flux profiles to the cloud top structures for the low-to-middle latitude region. (a) The cloud top altitude varies as shown in the legend, while the aerosol scale height is fixed to 4 km. (b) The aerosol scale height varies, during the cloud top altitude is fixed to 67 km.

polar regions, respectively, for the same range of the aerosol scale height (not shown in a figure). This results from non-monotonic temperature profiles, i.e. presence of temperature inversions and isothermal regions near the cloud tops.

The small aerosol scale height is responsible for a pronounced cooling rate peak at the cloud top (Fig. 8b, d, and f). This feature corresponds to sharp upper boundary of the cloud, making the cloud top an effective emitter of thermal radiation. The peak value increases from 5 K/day to 28 K/day as the aerosol scale height decreases from 6 km to 1 km (Fig. 8b). The cold collar and the polar region show similar trends in cooling rates with increasing peaks at the cloud tops as the aerosol scale height decreases (Fig. 8d and f).

Fig. 8a, c, and e shows that the cooling effects of the cloud top increase with its altitude. This is the most pronounced feature in the polar region because of small aerosol scale height, as discussed above. Decreasing with altitude heat capacity in the upper atmosphere is also related. For example, the net flux divergences near the cloud tops are about the same, between $Z=61$ km and $Z=70$ km in the polar region, but the peak of cooling rate increases from 9 K/day to 50 K/day. In addition, the cooling rate profiles (Fig. 8) demonstrate several local maxima and minima. These are caused by fluctuations in the observed temperature profiles, from small features to the temperature inversion layer, and strong CO_2 absorption bands. In the low-to-middle latitudes, cooling rate profile does not have distinct peak at the cloud top in Fig. 8a. This is caused by the large aerosol scale height, resulting in smooth change in the net flux near the cloud top as shown in Fig. 7a.

The results of sensitivity study convey interesting messages. The first one is that the cloud top altitude, more precisely the cloud top

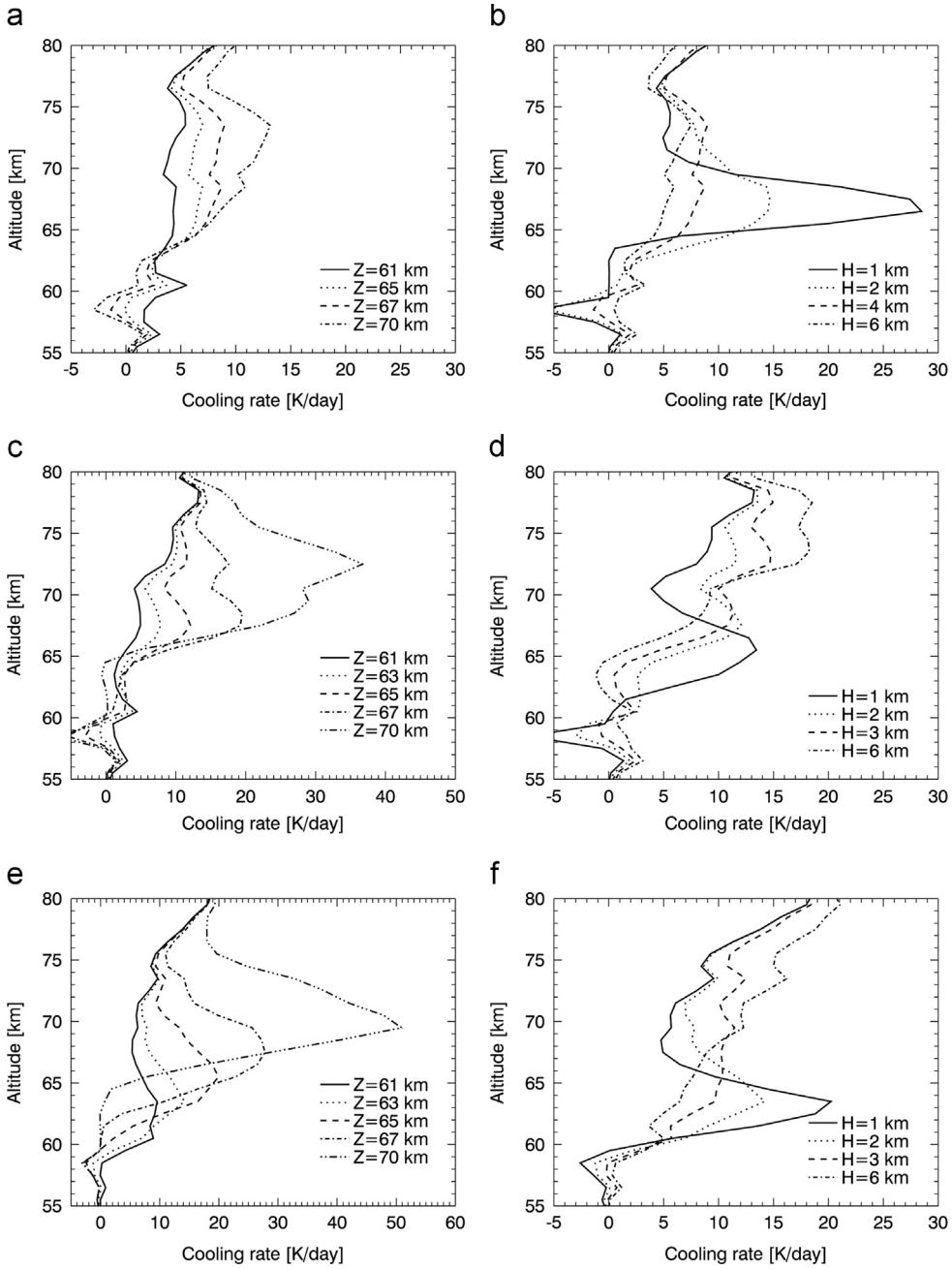

Fig. 8. Sensitivity of the thermal cooling rates to the cloud top structures for three latitudinal regions (Fig. 1). (a) and (b) are for the low-to-middle latitude region, (c) and (d) the cold collar region, and (e) and (f) the polar region. While one of cloud top structure parameters varies, another parameter is fixed to the value in Table 2. The cloud top altitude is a free parameter in (a) with a fixed aerosol scale height, and vice versa in (b). This setting is the same for other two regions; (c) and (d), and (e) and (f).

temperature, defines the outgoing emission. Secondly, there is strong latitudinal dependence due to the temperature structure variation. Thirdly, the aerosol scale height effectively controls sharpness of the cooling rate peak at the cloud top. The small aerosol scale height ($H \leq 2$ km) can generate a sharp cooling rate peak at the cloud top regardless of the temperature structure (Fig. 8b, d, and f). The sensitivity study also implies inter-relations and feedbacks between the cloud top structure and the temperature structure. For instance, sharp cloud top results in strong cooling rate peaks that can maintain temperature inversions ($H=1$ km case in Fig. 8d). This will be discussed in more detail in Section 4.

Fig. 9 presents the latitude–altitude field of thermal cooling rate derived from calculations in 18 latitudinal bins as described in Sections 2.1.1–2.1.3. This shows that strong thermal cooling dominates in the mesosphere while thermal emission contributes to heating below the clouds. Cooling rates at the cloud top increase from equator to pole following changes in the temperature and aerosol structure. In the polar region the cooling rate at the cloud top is about 10 K/day that is related to the small aerosol scale height in high latitudes and warm polar mesosphere. The mesosphere above the cloud top also experiences stronger cooling poleward of 50°S (>10 K/day at 68–80 km). This is caused by a combination of higher temperature at this altitudes and strong CO_2 absorptions. The local maximum of thermal heating at 57–60 km (also seen in Figs. 6 and 8) is likely due to discontinuity in the cloud extinction between the variable upper and fixed middle cloud layers in our cloud model (Fig. 2).

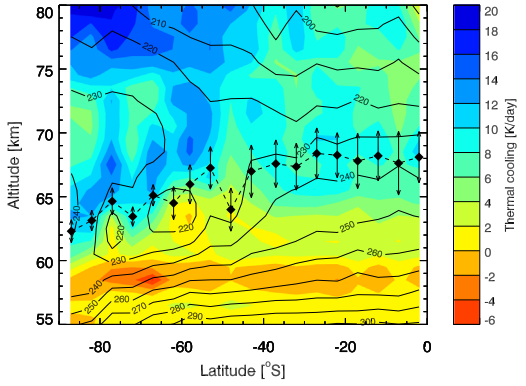

Fig. 9. Latitude–altitude field of thermal cooling in the Venus mesosphere. The cloud top altitudes are marked with black filled diamonds. Vertical arrows show the aerosol scale height (Table 1). The temperature field is shown in black contours.

3.2. Solar heating

Solar radiation is the second component in the radiative energy balance of the mesosphere. At the cloud top the direct solar flux quickly decreases, while diffused downward flux grows with decreasing altitude. Most of the solar flux is scattered back to space or absorbed by the clouds and gases. Only about 3% of the solar radiation that Venus received from the Sun reaches the surface. The upward solar flux is created by scattering in the atmosphere. The contribution of the clouds to heating is about 74% at the cloud top level at 0° solar zenith angle for the low-to-middle latitude cloud model (Table 2). The rest of the heating is due to gaseous species. Cloud's contribution is the strongest in the UV–visible range (~65%). It decreases quickly at longer wavelength contributing ~20% in the near-infrared range and ~15% in the infrared range. The strong UV–visible absorption is caused by the unknown UV absorber producing about 30–60% of the total solar heating effect, depending on the cloud top structure.

We performed sensitivity study for the solar spectral range for the same three latitude bins in which we studied the thermal range in Section 3.1. Solar local time was fixed at noon, while the solar zenith angles were 17.5° for the low-to-middle latitudes, 62.5° for the cold collar, and 87.5° for the polar region. Fig. 10 shows upward and downward fluxes in the low-to-middle latitudes as a function of the cloud top altitude (Fig. 10a) and the aerosol scale height (Fig. 10b). The sharp cloud top ($H=1$ km in Fig. 10b) produces a clear peak of diffused downward flux at the cloud top level. The upward fluxes increase with altitude within the cloud layer and remain constant above the cloud top. The comparison between Fig. 10a and b suggests that small aerosol scale height strongly affects solar flux profiles, resulting in maximum of both downward and upward fluxes at the cloud top.

Fig. 11 compares the solar heating rates at noon for the three latitudinal bins. Each panel demonstrates dependence of the heating rates on the cloud parameters. The higher cloud top results in stronger heating peak (Fig. 11a and c) for two reasons. The first one is that higher cloud has higher abundance of the UV absorber due to the assumption that it is located in the upper cloud layer (Section 2.1.4). The second reason is smaller heat capacity at higher altitude. Fig. 11b shows that small aerosol scale height ($H=1$ km) results in a strong heating peak of 94 K/day at the cloud top level, similar to the behavior of thermal cooling. We note that the solar heating at the cloud top (Fig. 11a and b) is more than twice as strong as thermal cooling, meaning that at noon the solar heating at the cloud top dominates. In the cold collar region (Fig. 11c and d), the solar heating rate at the cloud top are comparable to the thermal cooling rates. In the polar

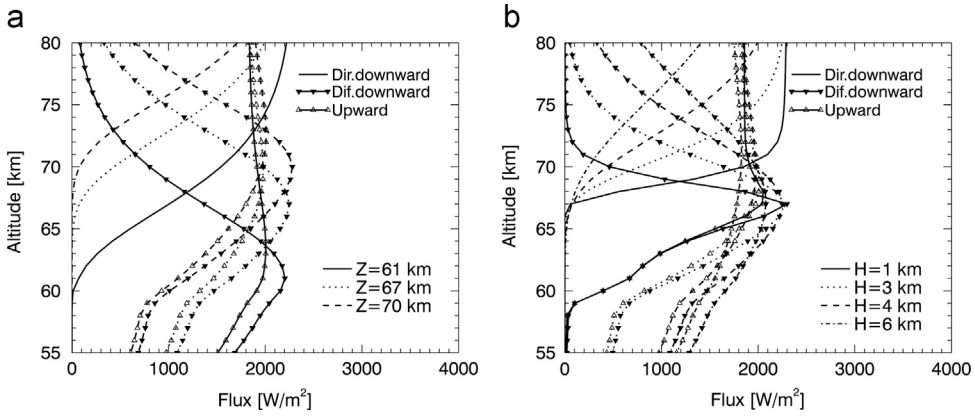

Fig. 10. Sensitivity of the solar flux to the cloud top structure in the low-to-middle latitude region. (a) The cloud top altitude varies from 61 km to 70 km, while the aerosol scale height is fixed to 4 km. (b) The aerosol scale height varies from 1 km to 6 km, while the cloud top altitude is fixed to 67 km. Direct downward (Dir. downward), diffused downward (Dif. downward), and upward flux profiles are shown separately.

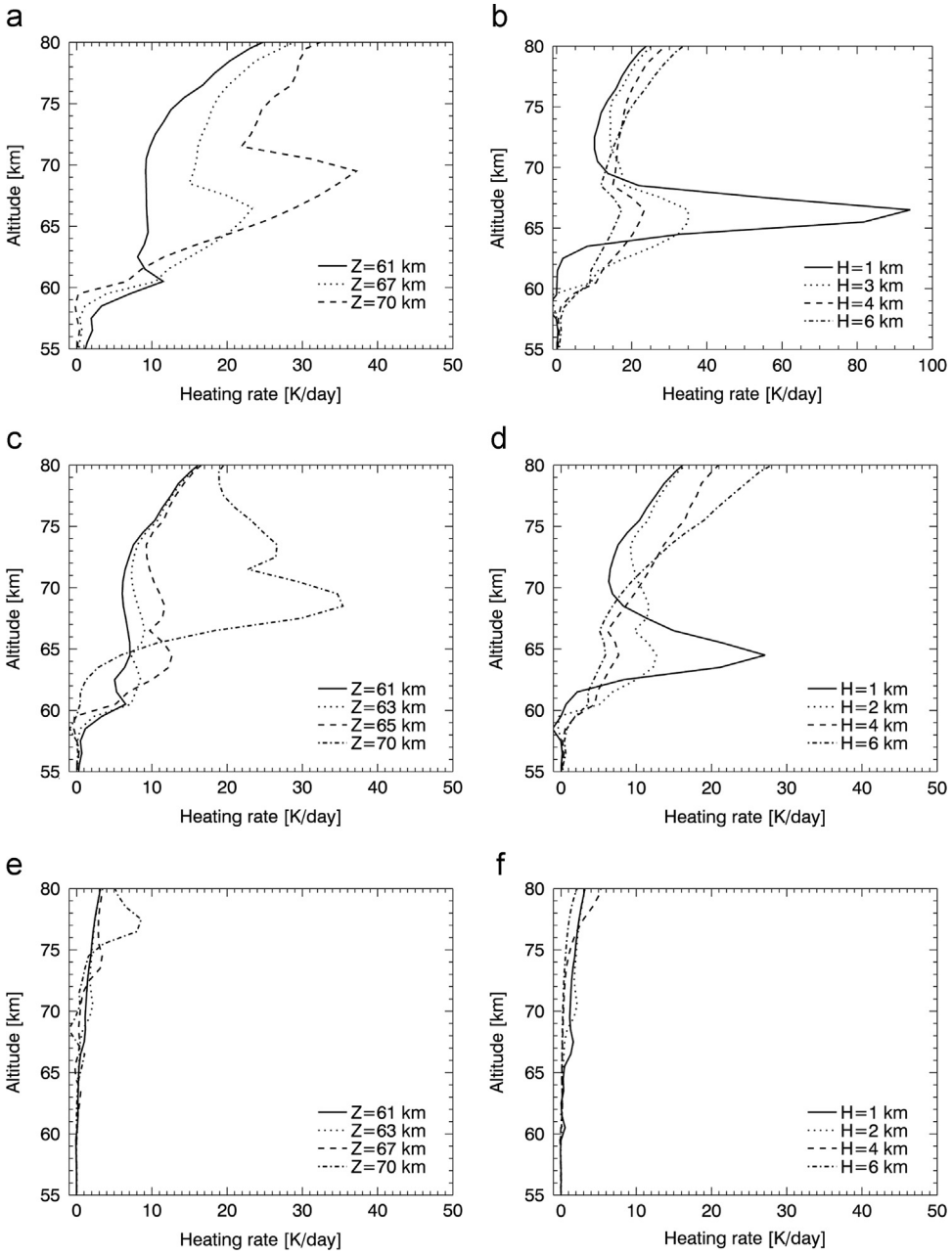

Fig. 11. Sensitivity of the solar heating profiles to the cloud top structure. The cloud top conditions in each panels are the same as in Fig. 8.

region (Fig. 11e and f), the solar heating becomes two orders of magnitude weaker than the thermal cooling.

The sensitivity studies for the cold collar region show two local peaks of the heating rate (Fig. 11c). One of them is located at the cloud top and is caused by the unknown UV absorber. Another peak above the cloud top is due to exponential vertical distribution of aerosol in the upper cloud, that contributes to scattering and absorption becoming significant at slant solar illumination. The secondary peak is present in the modelling with the scale height $H=2$ km (Fig. 11d). The sharp cloud top boundary ($H=1$ km) "removes" the secondary peak by clearing aerosol above the cloud altitude. The cases with $H>2$ km show that the heating rate gradually increases above the cloud top rather than creating a peak. The polar region receives very little solar energy, only 5% of that at low latitudes. Therefore, the solar heating is very weak. The heating at the cloud tops caused by the unknown UV absorber is less than 0.5 K/day. The secondary heating rate peak above the cloud top is ~2–8 K/day (Fig. 11e and f).

Local time dependence of the solar heating rate is shown in Fig. 12 for the 0–5°S latitudinal bin, cloud top altitude of 68 km and aerosol scale height of 4 km. As local time progresses from early morning to noon, the solar heating increases up to about 30 K/day at the cloud top (Fig. 12a). This peak is comparable to the values in Tomasko et al. (1985) at the sub-solar point. Fig. 12b suggests that from around 10 a.m. the solar heating exceeds the thermal cooling by ~20 K/day at the cloud top, thus indicating strong diurnal changes in radiative forcing at the cloud top at equator. This diurnal variability embeds interesting perspective on the cloud top morphology, which will be discussed in Section 4.

Diurnal average of the heating rate is calculated as follows:

$$\text{Diurnal averaged heating rate (lat)} = \frac{2\int_{6\text{ h}}^{12\text{ h}} \text{heating rate(lat}, t)\, dt}{24\text{ h}} \quad (5)$$

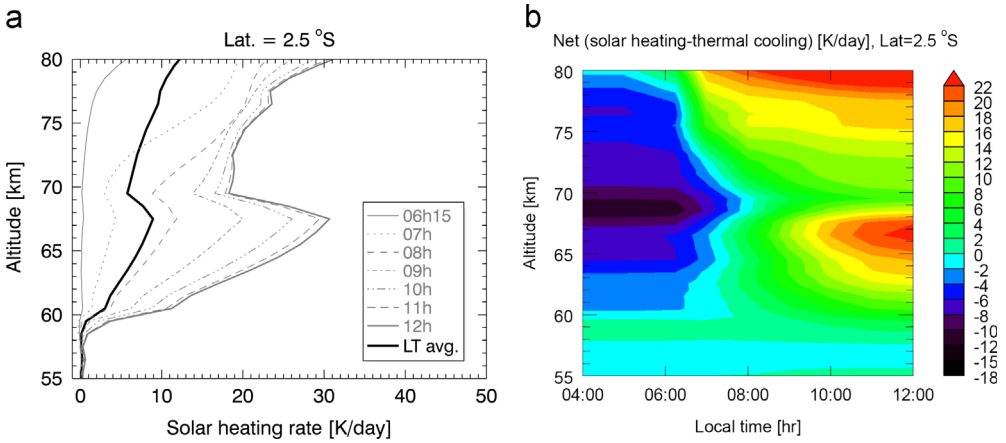

Fig. 12. (a) Heating rate profiles for different local times in the 0–5°S latitude bin (Table 1). Solar zenith angle changes from early morning (06:15) to noon (12:00). Solid line shows diurnally averaged solar heating rate (LT avg). (b) Net forcing field of local time and altitudes. Solar heating is the same as shown in (a), and is compared with thermal cooling calculated for the same cloud top structure.

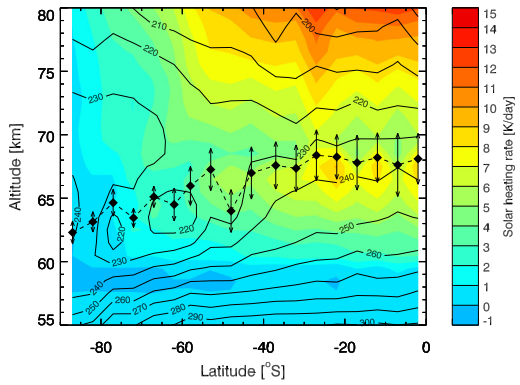

Fig. 13. Latitude–altitude field of diurnally averaged solar heating of the Venus mesosphere. The temperature and cloud top structures are the same as in Fig. 9.

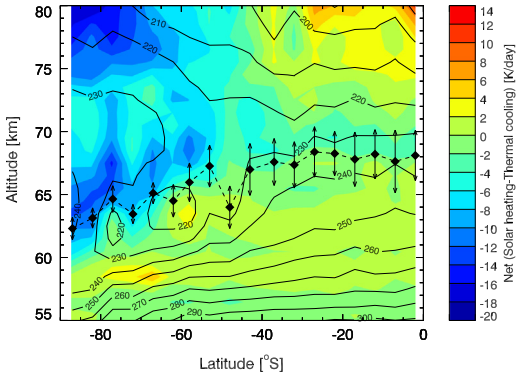

Fig. 14. Latitude–altitude field of the net radiative forcing in the Venus mesosphere. The temperature and cloud top structure are the same as in Figs. 9 and 13.

where t is the local time. A thick solid line in Fig. 12a shows this diurnal mean heating rate in this latitudinal bin.

Fig. 13 shows the meridional trend of the diurnally averaged solar heating rates. Solar heating near the cloud top is strong at low latitudes, and weaken towards high latitudes following decrease of the solar zenith angle. This figure shows strong solar heating peak at the cloud top, and solar heating in the mesosphere caused by the CO_2 absorption.

3.3. Net radiative forcing

Fig. 14 shows the net radiative energy budget which is the difference between solar heating (Fig. 13) and thermal cooling (Fig. 9). The net cooling is present at the cloud top at all latitudes, and increasing towards the south pole. We note however that the balance changes following diurnal variations of the solar heating. Net cooling prevails in the mesosphere at high latitudes, due to weakening of solar heating and enhancing of thermal cooling due to warmer atmosphere and sharp cloud tops. Right below the cloud top the radiative energy balance is close to zero. Fig. 14 also shows some weak net heating spots at 57–60 km in the cold collar region. These are due to peculiarities of the cloud model as discussed in Section 3.1. The net radiative forcing in the mesosphere gradually changes from heating to cooling from equator to pole, passing zero at 40–45°S. Therefore, the net radiative forcing alone would act to cool down the polar mesosphere and warming up the mesosphere at low latitudes. This suggests other mechanisms to maintain the observed mesospheric temperature contrasts, such as air rising at low latitudes and descending at high latitudes forming a global Hadley cell as proposed in the previous studies (Crisp, 1989; Crisp and Titov, 1997; Titov et al., 2007).

We estimate zonally averaged vertical and meridional winds, which can compensate the net radiative energy imbalance in Fig. 14, assuming adiabatic air motions. Transformed Eulerian mean in a spherical coordinate is

$$\frac{\partial \overline{T}}{\partial t}+\frac{\overline{v}^*}{a}\frac{\partial \overline{T}}{\partial \phi}+\overline{w}^*\left(N^2\frac{H}{R}\right)=\frac{\overline{J}}{c_p} \tag{6}$$

$$\frac{1}{a\cos\phi}\frac{\partial(\overline{v}^*\cos\phi)}{\partial\phi}+\frac{\partial(\rho_o\overline{w}^*)}{\partial z}=0 \tag{7}$$

where N^2 is the buoyancy frequency, H is the atmospheric scale height (different from the aerosol scale height), R is the gas constant, ϕ is latitude, and $\overline{w}^*$ and $\overline{v}^*$ are the vertical and meridional wind speeds in the residual mean circulation (following Holton, 1992, and Santee and Crisp, 1995), ignoring wave heatings. z is in the log–pressure coordinate, defined as $z\equiv -H\ln(p/p_s)$, where p_s is the surface pressure. The density profile is $\rho_o(z)=\rho_s\exp(-z/H)$, where ρ_s is the surface density. We assume steady zonal mean temperature $\partial\overline{T}/\partial t=0$. Assessment of the terms in Eq. (6) showed that the second term describes meridional heat advection is one order of magnitude smaller than the third term describing adiabatic heating except the cold collar. The system of Eqs. (6) and (7) was solved numerically by finite difference method on the grid with latitudinal step of 5° and for the atmosphere divided into 81 equal log–pressure steps from 89,275 mbar to 0.002 mbar.

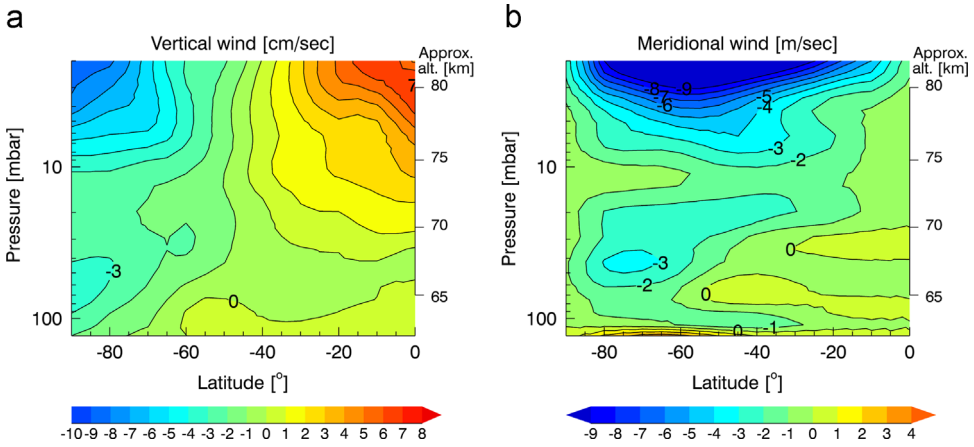

Fig. 15. (a) Estimated vertical wind velocity to compensate the net radiative forcing in Fig. 14. (b) Estimated zonal-average meridional wind. See text for details.

Fig. 15 shows smoothed fields of vertical and meridional winds derived from Eqs. (6) and (7). At high latitudes, the downward wind velocity is about 3 cm/s at the cloud top increasing with altitude. In equatorial region, weak upward motions exist below the cloud top significantly increasing above 70 km. Fig. 15b shows that poleward wind prevails in the mesosphere. This wind speed is consistent with Crisp (1989). Below and near the cloud top, equator ward winds with the speed of up to ~1 m/s is present. This result qualitatively supports the presence of the Hadley circulation in the mesosphere (Crisp, 1989; Crisp and Titov, 1997). We note, however, that the 2-D model can provide only crude assessment of the atmospheric dynamics and results in lower meridional wind than the observed at the cloud top level (~10 m/s) (Sánchez-Lavega et al., 2008; Khatuntsev et al., 2013; Kouyama et al., 2013).

4. Conclusion

We calculated the thermal cooling and solar heating rates for a set of atmospheric models based on the Venus Express observations. The results show that variations of the cloud top structure cause significant changes in the radiative forcing. Extending the cloud layer upward decreases the outgoing thermal flux and enhances mesospheric cooling (Figs. 7 and 8). Small aerosol scale height results in strong peak of cooling at the cloud top (Fig. 8). This behavior can have a remarkable radiative effect in the cold collar and at high latitudes where small aerosol scale height is often observed (Lee et al., 2012), so that the atmosphere at the cloud top level can experience enhanced thermal cooling at night. Grassi et al. (2010) retrieved the temperature field as a function of latitude and local solar time based on observations by VIRTIS spectrometer on board Venus Express. Their result showed a clear cooling trend at high latitudes near the cloud top (~65 km) during night, that can be caused by thermal cooling. Moreover, the cloud top with small aerosol scale height coincides with the minimum of temperature inversion in the cold collar region (Lee et al., 2012). This suggests a likely radiative origin of the temperature inversion layer. The dynamic phenomena, like the downwelling branch of Hadley circulation (Tellmann et al., 2009), might also play a role in the formation of the sharp cloud top.

The analysis also revealed distinct solar heating at the sub-solar point that dominates the radiative net forcing at noon (Fig. 12). The sensitivity study shows that variation of the cloud top altitude would alter the solar heating rate. For instance, the raising of the cloud top altitude from 67 km to 70 km increases the heating rate at the cloud top level about 50% (Fig. 11a). In addition, horizontally uneven distribution of the unknown UV absorbers would cause spatially inhomogeneous solar heating of the cloud top since the UV absorber is responsible for about half of the total solar heating at the cloud top. The UV images taken by camera onboard Venus Express and Pioneer Venus showed convective-like small cells at low latitudes in the afternoon. These features are probably caused by strong heating at the cloud tops, as the convective motion at the lower and middle cloud layers is suppressed at the sub-solar point (Imamura et al., 2014). Toigo et al. (1994) suggested a thin layer of solar absorption may trigger convective motions at the cloud top. Our results also indicate that the strong solar heating at noon time combined with zonal and horizontal variations of the UV absorber distribution can be responsible for the observed features. In our future study we will use a fluid dynamic model calculation to verify this effect.

Our modelling suggests strong meridional contrasts of net radiative budget in the mesosphere with excessive net heating at low latitudes and net cooling in the cold collar and polar regions (Fig. 14). This net forcing is strong enough to support the Hadley-type meridional circulation in the mesosphere with upwelling at the equator and downwelling at the pole with vertical wind speed of few cm/s. Global circulation modeling would be helpful to understand the link between dynamics and radiative forcing in the Venus mesosphere.

Acknowledgments

Y.J. Lee would like to thank Dr. Takeshi Imamura for discussions and comments. Anonymous reviewers gave helpful comments to improve this paper.

References

Barker, E.S., Woodman, J.H., Perry, M.A., Hapke, B.A., Nelson, R., 1975. Relative spectrophotometry of Venus from 3067 to 5960 Å. J. Atmos. Sci. 32 (June), 1205–1211.

Bullock, M.A., 1997. The Stability of Climate on Venus [Ph.D. thesis]. University of Colorado, Boulder.

Burch, D.E., Gryvnak, D.A., Patty, R.R., Bartky, C.E., 1969. Absorption of infrared radiant energy by CO_2 and H_2O. IV. Shapes of collision-broadened CO_2 lines. J. Opt. Soc. Am. (1917–1983) 59, 267.

Chapman, S., 2007. Fortran 95/2003 for Scientists and Engineers, 3rd edition McGraw-Hill Science/Engineering/Math, USA.

Crisp, D., 1986. Radiative forcing of the venus mesosphere. I. Solar fluxes and heating rates. Icarus 67 (September), 484–514.

Crisp, D., 1989. Radiative forcing of the Venus mesosphere. II. Thermal fluxes, cooling rates, and radiative equilibrium temperatures. Icarus 77 (February), 391–413.

Crisp, D., Titov, D., 1997. The thermal balance of the venus atmosphere. In: Bougher, S.W., Hunten, D.M., Phillips, R.J. (Eds.), Venus II: Geology, Geophysics, Atmosphere, and Solar Wind Environment. The University of Arizona Press, Tucson, pp. 353–384.
Esposito, L.W., 1980. Ultraviolet contrasts and the absorbers near the venus cloud tops. J. Geophys. Res.: Sp. Phys. 85 (A13), 8151–8157.
Evans, K.F., 1998. The spherical harmonics discrete ordinate method for three-dimensional atmospheric radiative transfer. J. Atmos. Sci. 55 (February), 429–446.
Fedorova, A., Korablev, O., Vandaele, A.-C., Bertaux, J.-L., Belyaev, D., Mahieux, A., Neefs, E., Wilquet, W.V., Drummond, R., Montmessin, F., Villard, E., 2008. HDO and H_2O vertical distributions and isotopic ratio in the Venus mesosphere by solar occultation at infrared spectrometer on board venus express. J. Geophys. Res. (Planets) 113.
Gierasch, P.J., Goody, R.M., Young, R.E., Crisp, D., Edwards, C., Kahn, R., Rider, D., del Genio, A., Greeley, R., Hou, A., Leovy, C.B., McCleese, D., Newman, M., 1997. The general circulation of the venus atmosphere: an assessment. In: Bougher, S.W., Hunten, D.M., Phillips, R.J. (Eds.), Venus II: Geology, Geophysics, Atmosphere, and Solar Wind Environment. The University of Arizona Press, Tucson, pp. 459–500.
Goody, R.M., Yung, Y.L., 1989. Atmospheric Radiation: Theoretical Basis, 2nd edition Oxford University Press, New York.
Grassi, D., Migliorini, A., Montabone, L., Lebonnois, S., Cardesìn-Moinelo, A., Piccioni, G., Drossart, P., Zasova, L.V., 2010. Thermal structure of Venusian nighttime mesosphere as observed by VIRTIS-Venus Express. J. Geophys. Res. (Planets) 115 (September), 9007.
Hansen, J.E., Travis, L.D., 1974. Light scattering in planetary atmospheres. Sp. Sci. Rev. 16 (October), 527–610.
Haus, R., Kappel, D., Arnold, G., 2014. Atmospheric thermal structure and cloud features in the southern hemisphere of Venus as retrieved from VIRTIS/VEX radiation measurements. Icarus 232 (April), 232–248.
Häusler, B., Pätzold, M., Tyler, G.L., Simpson, R.A., Bird, M.K., Dehant, V., Barriot, J.-P., Eidel, W., Mattei, R., Remus, S., Selle, J., Tellmann, S., Imamura, T., 2006. Radio science investigations by VeRa onboard the Venus Express spacecraft. Planet. Sp. Sci. 54 (November), 1315–1335.
Holton, J.R., 1992. An Introduction to Dynamic Meteorology, 3rd edition Academic Press, San Diego.
Ignatiev, N.i., Moroz, V.i., Zasova, L.V., Khatuntsev, I.v., 1999. Water vapour in the middle atmosphere of Venus: an improved treatment of the Venera 15 ir spectra. Planet. Sp. Sci. 47 (August), 1061–1075.
Ignatiev, N.I., Titov, D.V., Piccioni, G., Drossart, P., Markiewicz, W.J., Cottini, V., Roatsch, T., Almeida, M., Manoel, N., 2009. Altimetry of the Venus cloud tops from the Venus Express observations. J. Geophys. Res. Planets 114 (August).
Imamura, T., Higuchi, T., Maejima, Y., Takagi, M., Sugimoto, N., Ikeda, K., Ando, H., 2014. Inverse insolation dependence of Venus' cloud-level convection. Icarus 228 (January), 181–188.
Khatuntsev, I.V., Patsaeva, M.V., Titov, D.V., Ignatiev, N.I., Turin, A.V., Limaye, S.S., Markiewicz, W.J., Almeida, M., Roatsch, T., Moissl, R., 2013. Cloud level winds from the Venus Express Monitoring Camera imaging. Icarus 226 (1), 140–158.
Knollenberg, R.G., Hunten, D.M., 1980. The microphysics of the clouds of Venus - results of the Pioneer Venus particle size spectrometer experiment. J. Geophys. Res. 85 (December), 8039–8058.
Kouyama, T., Imamura, T., Nakamura, M., Satoh, T., Futaana, Y., 2013. Long-term variation in the cloud-tracked zonal velocities at the cloud top of Venus deduced from Venus Express VMC images. J. Geophys. Res. (Planets) 118 (January), 37–46.
Lebonnois, S., Hourdin, F., Eymet, V., Crespin, A., Fournier, R., Forget, F., 2010. Superrotation of Venus' atmosphere analyzed with a full general circulation model. J. Geophys. Res. (Planets) 115 (June), 6006.
Lee, C., Richardson, M.I., 2011. A discrete ordinate, multiple scattering, radiative transfer model of the venus atmosphere from 0.1 to 260 μm. J. Atmos. Sci. 68 (June), 1323–1339.
Lee, Y.J., Titov, D.V., Tellmann, S., Piccialli, A., Ignatiev, N., Pätzold, M., Häusler, B., Piccioni, G., Drossart, P., 2012. Vertical structure of the Venus cloud top from the VeRa and VIRTIS observations onboard Venus Express. Icarus 217 (February), 599–609.
Levoni, C., Cervino, M., Guzzi, R., Torricella, F., 1997. Atmospheric aerosol optical properties: a database of radiative characteristics for different components and classes. Appl. Opt. 36 (October), 8031–8041.
Limaye, S.S., 2007. Venus atmospheric circulation: known and unknown. J. Geophys. Res. (Planets) 112 (April), 4.
Meadows, V.S., Crisp, D., 1996. Ground-based near-infrared observations of the Venus nightside: the thermal structure and water abundance near the surface. J. Geophys. Res. 101, 4595–4622.
Migliorini, A., Grassi, D., Montabone, L., Lebonnois, S., Drossart, P., Piccioni, G., 2012. Investigation of air temperature on the nightside of Venus derived from VIRTIS-H on board Venus-Express. Icarus 217 (February), 640–647.
Moroz, V.I., Ekonomov, A.P., Golovin, Y.M., Moshkin, B.E., San'ko, N.F., 1983. Solar radiation scattered in the Venus atmosphere - The Venera 11, 12 data. Icarus 53 (March), 509–537.
Moroz, V.I., Ekonomov, A.P., Moshkin, B.E., Revercomb, H.E., Sromovsky, L.A., Schofield, J.T., 1985. Solar and thermal radiation in the Venus atmosphere. Adv. Sp. Res. 5, 197–232.
Moskalenko, N.I., Parzhin, S.N., 1981. Investigation of absorption spectra of carbon dioxide under high pressures. in: Proceedings of the 6th All-Union Symposium on the Propagation of the Laser Radiation in the Atmosphere. IOA SO AN SSSR, Tomsk, pp. 110–113 [In Russian].
Palmer, K.F., Williams, D., 1975. Optical constants of sulfuric acid - Application to the clouds of Venus. Appl. Opt. 14 (January), 208–219.
Pätzold, M., Häusler, B., Bird, M.K., Tellmann, S., Mattei, R., Asmar, S.W., Dehant, V., Eidel, W., Imamura, T., Simpson, R.A., Tyler, G.L., 2007. The structure of Venus' middle atmosphere and ionosphere. Nature 450 (November), 657–660.
Pollack, J.B., 1967. Rayleigh scattering in an optically thin atmosphere and its application to Martian topography. Icarus 7, 42–46.
Pollack, J.B., Dalton, J.B., Grinspoon, D., Wattson, R.B., Freedman, R., Crisp, D., Allen, D.A., 1993. Near-infrared light from Venus' nightside - A spectroscopic analysis. Icarus 103 (May), 1–42.
Pollack, J.B., Ragent, B., Boese, R.W., Tomasko, M.G., Blamont, J., Knollenberg, R.G., Esposito, L.W., Stewart, A.I., Travis, L., 1979. Nature of the ultraviolet absorber in the Venus clouds - Inferences based on Pioneer Venus data. Science 205 (July), 76–79.
Pollack, J.B., Toon, O.B., Whitten, R.C., Boese, R., Ragent, B., Tomasko, M., Esposito, L., Travis, L., Wiedman, D., 1980. Distribution and source of the uv absorption in venus' atmosphere. J. Geophys. Res. 85 (December), 8141–8150.
Ragent, B., Esposito, L.W., Tomasko, M.G., Marov, M.I., Shari, V.P., 1985. Particulate matter in the Venus atmosphere. Adv. Sp. Res. 5, 85–115.
Rothman, L.S., Gordon, I.E., Barbe, A., Benner, D.C., Bernath, P.F., Birk, M., Boudon, V., Brown, L.R., Campargue, A., Champion, J.-P., Chance, K., Coudert, L.H., Dana, V., Devi, V.M., Fally, S., Flaud, J.-M., Gamache, R.R., Goldman, A., Jacquemart, D., Kleiner, I., Lacome, N., Lafferty, W.J., Mandin, J.-Y., Massie, S.T., Mikhailenko, S.N., Miller, C.E., Moazzen-Ahmadi, N., Naumenko, O.V., Nikitin, A.V., Orphal, J., Perevalov, V.I., Perrin, A., Predoi-Cross, A., Rinsland, C.P., Rotger, M., Šimečková, M., Smith, M.A.H., Sung, K., Tashkun, S.A., Tennyson, J., Toth, R.A., Vandaele, A.C., Vander Auwera, J., 2009. The HITRAN 2008 molecular spectroscopic database. J. Quant. Spectrosc. Radiat. Transf. 110 (June), 533–572.
Sánchez-Lavega, A., Hueso, R., Piccioni, G., Drossart, P., Peralta, J., Pérez-Hoyos, S., Wilson, C.F., Taylor, F.W., Baines, K.H., Luz, D., Erard, S., Lebonnois, S., 2008. Variable winds on Venus mapped in three dimensions. Geophys. Res. Lett. 35 (July), 13204.
Santee, M.L., Crisp, D., 1995. Diagnostic calculations of the circulation in the Martian atmosphere. J. Geophys. Res. 100 (March), 5465–5484.
Seiff, A., Schofield, J.T., Kliore, A.J., Taylor, F.W., Limaye, S.S., 1985. Models of the structure of the atmosphere of Venus from the surface to 100 kilometers altitude. Adv. Sp. Res. 5, 3–58.
Takagi, M., Matsuda, Y., 2007. Effects of thermal tides on the Venus atmospheric superrotation. J. Geophys. Res. Atmos. 112 (May), 9112.
Tanaka, M., Yamanouchi, T., 1977. Absorption properties of the near infrared CO_2 bands. J. Quant. Spectrosc. Radiat. Transf. 17 (March), 421–432.
Taylor, F.W., 2006. Venus before venus express. Planet. Sp. Sci. 54 (November), 1249–1262.
Taylor, F.W., Hunten, D.M., Ksanfomalit, L.V., 1983. The thermal balance of the middle and upper atmosphere of Venus. In: Hunten, D.M., Colin, L., Donahue, T.M., Moroz, V.I. (Eds.), Venus. The University of Arizona Press, Tucson, pp. 650–680.
Tellmann, S., Pätzold, M., Häusler, B., Bird, M.K., Tyler, G.L., 2009. Structure of the Venus neutral atmosphere as observed by the Radio Science experiment VeRa on Venus Express. J. Geophys. Res. (Planets) 114 (April).
Titov, D.V., Bullock, M.A., Crisp, D., Renno, N.O., Taylor, F.W., Zasova, L.V., 2007. Radiation in the atmosphere of venus. In: Esposito, L., Stofan, E.R., Cravens, T.E. (Eds.), Exploring Venus as a Terrestrial Planet, Geophysical Monograph Series. American Geophysical Union, Washington, DC.
Titov, D.V., Haus, R., 1997. A fast and accurate method of calculation of gaseous transmission functions in planetary atmospheres. Planet. Sp. Sci. 45 (March), 369–377.
Toigo, A., Gierasch, P.J., Smith, M.D., 1994. High resolution cloud feature tracking on Venus by Galileo. Icarus 109 (June), 318–336.
Tomasko, M.G., Doose, L.R., Smith, P.H., 1985. The absorption of solar energy and the heating rate in the atmosphere of Venus. Adv. Sp. Res. 5, 71–79.
Tomasko, M.G., Doose, L.R., Smith, P.H., Odell, A.P., 1980a. Measurements of the flux of sunlight in the atmosphere of Venus. J. Geophys. Res. 85 (December), 8167–8186.
Tomasko, M.G., Smith, P.H., Suomi, V.E., Sromovsky, L.A., Revercomb, H.E., Taylor, F.W., Martonchik, D.J., Seiff, A., Boese, R., Pollack, J.B., Ingersoll, A.P., Schubert, G., Covey, C.C., 1980b. The thermal balance of Venus in light of the Pioneer Venus mission. J. Geophys. Res. 85 (December), 8187–8199.
Tonkov, M.V., Filippov, N.N., Bertsev, V.V., Bouanich, J.P., van-Thanh, N., Brodbeck, C., Hartmann, J.M., Boulet, C., Thibault, F., Le Doucen, R., 1996. Measurements and empirical modeling of pure CO_2 absorption in the 2.3-m region at room temperature: far wings, allowed and collision-induced bands. Appl. Opt. 35 (August), 4863–4870.
Winters, B., Silverman, S., Benedict, W.S., 1964. Line shape in the wing beyond the band head of the 4.3 μ m band of CO_2. J. Quant. Spectrosc. Radiat. Transf. 4 (August), 527–537.
Wiscombe, W.J., 1980. Improved Mie scattering algorithms. Appl. Opt. 19 (May), 1505–1509.
Wu, C.Y.R., Yang, B.W., Chen, F.Z., Judge, D.L., Caldwell, J., Trafton, L.M., 2000. Measurements of high-, room-, and low-temperature photoabsorption cross sections of SO_2 in the 2080- to 2950-Å region, with application to Io. Icarus 145 (1), 289–296.
Zasova, L.V., Ignatiev, N., Khatuntsev, I., Linkin, V., 2007. Structure of the venus atmosphere. Planet. Sp. Sci. 55 (October), 1712–1728.